Nanoscale

PAPER

View Article Online
View Journal | View Issue

Cite this: *Nanoscale*, 2023, **15**, 1109

Highly stable lanthanide-doped $CsPbI_3$ perovskite nanocrystals with near-unity quantum yield for efficient red light-emitting diodes†

Wenlin Xia,[a] Zhenwei Ren, *[a] Zhishuai Zheng,[a] Chengzhao Luo,[a] Jie Li,[a] Wenchen Ma,[a] Xin Zhou[a] and Yu Chen *[a,b]

$CsPbI_3$ perovskite nanocrystals (NCs) are gaining popularity as promising photoactive materials for optoelectronic devices. However, their poor phase stability has caused substantial limitations in their practical application. Herein, the small-sized rare earth La cation is strategically introduced to fundamentally improve the NC phase stability against the environment, heat, and UV radiation by the partial substitution of Pb ions to suppress structural distortion and increase the formation energy. The strong interaction between La and I of the octahedra has been demonstrated to enable the effective suppression of the trap states, which promotes strengthened radiative recombination for a near-unity photoluminescence quantum yield (PLQY) of 99.3%. High energy bands have also been found for the La-doped NCs to narrow down the energy barrier for efficient hole injection. The superior optoelectronic properties of La-doped NCs promote great improvements in the perovskite light-emitting diode (PeLED) performances with a 5-fold improvement in external quantum efficiency (EQE) from 1.19 to 6.01% and 2-fold longer lifetime from 1451 to 2956 s. This work provides an effective method for small-sized metal ion-doped $CsPbI_3$ NCs to realize high emission efficiency and phase stabilization for efficient PeLEDs.

Received 11th November 2022,
Accepted 13th December 2022

DOI: 10.1039/d2nr06317d

rsc.li/nanoscale

Introduction

All-inorganic cesium lead halide perovskite ($CsPbX_3$, X = Cl, Br, I) nanocrystals (NCs) are competitive candidates for the next-generation optoelectronic materials due to their arresting optical properties, such as tunable band gap, narrow emission width, high defect tolerance, and high photoluminescence quantum yields (PLQYs).[1–5] In particular, significant interest in $CsPbX_3$ NCs for the construction of the perovskite light-emitting diodes (PeLEDs) and impressive external quantum efficiencies (EQEs) have been achieved for green, red, and blue PeLEDs through the efforts of perovskite material optimization and device structure design.[6–9] However, there is concern about the intrinsic instability of the crystal phase of the $CsPbX_3$ NCs, particularly for the $CsPbI_3$ NCs, which undoubtedly sets substantial limitations on the further improvement of the device performance and subsequent commercial applications.

The photoactive cubic $CsPbI_3$ NCs exhibit the worst stability among the $CsPbX_3$ NCs (*i.e.*, $CsPbBr_3$, $CsPbCl_3$) due to their having the smallest tolerance factor (t) determined from the equation of $t = (r_A + r_X)/[\sqrt{2}(r_B + r_X)]$, where r_A, r_B, and r_X are the ionic radii of the respective ions in the ABX_3 formula.[10] The value of t has been adopted to evaluate the structural stability of $CsPbX_3$ NCs, where the ideal cubic structure is formed at the value of t = 1. $CsPbI_3$ NCs have a small t of around 0.89, which results in serious structural distortion for a metastable phase.[11,12] The cubic $CsPbI_3$ NCs tend to transform into the non-photoactive orthorhombic (δ) phase under humid or thermal stress conditions.[13–15] The distorted structure of cubic $CsPbI_3$ NCs also prompts the formation of massive trap states during crystal growth, which undoubtedly aggravates the luminescence performance of $CsPbI_3$ NCs. Fortunately, substantial efforts have been made to improve the stability of cubic $CsPbI_3$ NCs as well as the emission efficiency.[16–18] For example, the steric ligands (*e.g.*, quaternary amine, thiol ligands) with strong coupling for surface atoms of lead-halide octahedral were adopted to diminish the NC octahedral tilting for improved phase stability.[19] Meanwhile, the strategy of surface encapsulation with polymers (*e.g.*, polyvinylpyrrolidone, polymethyl methacrylate dichloromethane)[20] and metal oxides (*e.g.*, SiO_2, Al_2O_3)[21,22] was also employed to inhibit the environment-induced phase transition.

[a]*School of Optoelectronic Science and Engineering & Collaborative Innovation Center of Suzhou Nano Science and Technology, Soochow University, Suzhou 215006, China. E-mail: zhwren@suda.edu.cn, chenyu_ny@suda.edu.cn*
[b]*National University of Singapore Suzhou Research Institute, Dushu Lake Science and Education Innovation District, Suzhou 215123, China*

† Electronic supplementary information (ESI) available. See DOI: https://doi.org/10.1039/d2nr06317d

Although the above strategies prompt various degrees of stability enhancement, the structure distortion of cubic $CsPbI_3$ NCs remains to be solved fundamentally. In addition, the insulating nature of the polymers and metal oxides undoubtedly prohibits the application of NCs in the fabrication of efficient PeLEDs. Excitingly, the strategy of ion doping provides another method for stabilizing the $CsPbI_3$ NCs by increasing the tolerance factor to fundamentally reduce structure distortion.[23] For example, organic cations with large ionic radii (*e.g.*, methylamine: MA, formamidine: FA) were doped into the $CsPbI_3$ bulk film to increase the tolerance factor and reduce the structure distortion for stable $FA_{1-x}Cs_xPbI_3$.[24] However, the issue of decomposition at high temperatures for these organic cations limits their use in synthesizing $CsPbI_3$ NCs (>160 °C).[1] Small-sized halide doping was also employed by incorporating Br ions into $CsPbI_3$ NCs to form mixed halide $CsPbI_xBr_{3-x}$ NCs for suppressed structural distortion.[25] Similarly, the problem of ion migration of Br and I would cause phase separation under some harsh conditions (*e.g.*, high temperature, large electric field) and results in the degradation of optoelectronic performance.[26] Metal ion doping for partial replacement of Pb ions with alkaline earth and/or transition metal elements, such as Mg^{2+},[27] Ni^{2+},[28,29] Zn^{2+},[30,31] Ca^{2+},[32] and Sr^{2+},[33,34] can avoid the issues of thermal decomposition, phase separation, and poor conductivity, thus serving as an effective way to stabilize $CsPbI_3$ NCs for efficient device performance.

In this work, inspired by the merits of metal ion doping, La, the rare earth element with a small ionic radius (103 pm for La^{3+} as compared to 119 pm for Pb^{2+}), has been introduced into the lattice of $CsPbI_3$ NCs to improve their structural stability by the partial substitution of Pb ions for enhanced formation energy. Meanwhile, the strong interaction between La and I of the octahedra greatly reduces the trap states, promoting a large enhancement of emission efficiency with PLQY remarkably increased from 70.1% to a near-unity value of 99.3%. The La-doped $CsPbI_3$ NCs also exhibit efficient carrier transport by improving the energy band for a narrowed hole injection barrier. The superior optoelectronic properties for La-doped $CsPbI_3$ NCs provide the benefits of a great enhancement of the PeLED performance with a 5-fold improvement in external quantum efficiency (EQE) from 1.19 to 6.01%, a remarkable increase in luminance from 62 to 592 cd m^{-2}, a prolonged operational lifetime from 1451 to 2956 s, and a distinct decrease in turn-on voltage from 5.5 to 4.9 V. Consequently, this work provides an effective method for new-type metal ion doping by partially substituting Pb for high-performance $CsPbI_3$ PeLEDs.

Results and discussion

The pristine $CsPbI_3$ NCs were synthesized by the hot-injection method according to previous reports.[35] The La-doped $CsPbI_3$ NCs were prepared by adding different amounts of lanthanum acetylacetonate ($La(acac)_3$) into the perovskite precursors followed by the injection of Cs precursor at high temperature as illustrated in Fig. 1. Details are shown in the Experimental section. The ionic radius of La^{3+} of around 103 pm is smaller than that of Pb^{2+} (119 pm), which causes the contraction of the NC lattice and thus the relaxation of the structure distortion when La^{3+} is incorporated into the perovskite octahedra (Fig. 1b). The first-principles calculations based on density functional theory (DFT) were performed to investigate the effects of La-dopant on the NC energy band (Fig. 1c and d). The density of states (DOS) of pristine and La-doped NCs show

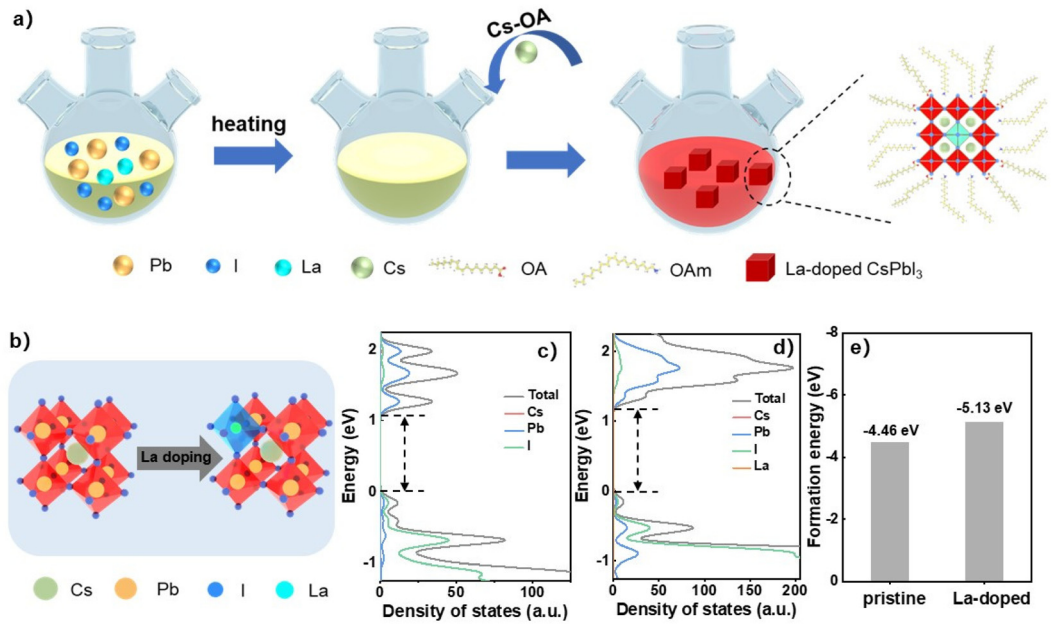

Fig. 1 (a) Illustration of the synthesis process of La-doped $CsPbI_3$ NCs and (b) the substitution of Pb with La. The first-principles calculations: the density of states (DOS) of (c) pristine and (d) La-doped NCs and (e) the calculated formation energy of the NCs.

that their conduction band (CB) and valence band (VB) are mainly derived from the contribution of Pb and I atoms, while the Cs atom has no significant effect on the energy band. There is also no significant energy state variation induced by the La atom. However, a distinct increase in band-gap (E_g) is observed for La-doped NCs due to the lattice contraction after La doping, and the enlarged E_g for La-doped NCs will induce the blue-shifting of the emission peaks, which is described later. The calculated E_g of 1.10 eV for $CsPbI_3$ NCs is smaller than the reported value of 1.73 eV (ref. 36) due to the typically underestimated E_g obtained from the method of the generalized gradient approximation (GGA) and the Perdew–Burke–Ernzerhof (PBE) exchange–correlation function.[37,38] The formation energy (H_f) of the NCs was also calculated based on DFT *via* the equation $H_f = E - \sum \mu_i x_i$, where E is the total energy of the perovskites, μ_i is the chemical potential of the element i (*e.g.*, Cs, Pb, I), and x_i is the quantity of element i in the perovskites.[39] The total energy of pristine and La-doped $CsPbI_3$ NCs are −13.55 and −14.24 eV, respectively. The ratio of La is fixed at 1/64 (*i.e.*, $CsPb_{63/64}La_{1/64}I_3$) in the calculation system to detect the difference between pristine and La-doped NCs, which is near the actual ratio of La as discussed later and a ratio lower than 1/64 is useless for DFT calculations. The chemical potential of Cs, Pb, I, and La are −0.86, −3.70, −1.51, and −5.20 eV, respectively. Thus, the calculated formation energies for pristine and La-doped $CsPbI_3$ NCs are −4.46 and −5.13 eV, respectively (Fig. 1e). The absolute value of the formation energy for the pristine NCs is 4.46 eV, which increases by 0.67 eV for La-doped NCs (5.13 eV). Since the larger absolute value of H_f indicates greater energetic stability for the NCs, the result verifies that the partial substitution of Pb with La is thermodynamically favored. The strategy of La doping promotes superior optoelectronic properties for the NCs, which will be carefully discussed in the following sections.

The ratio of La/Pb in La-doped $CsPbI_3$ NCs was calibrated by inductively coupled plasma optical emission spectrometry (ICP-OES) (Table S1†), in which mole ratios of 0.18%, 0.51%, 0.67%, and 0.96% were obtained for 5%, 10%, 15%, and 20% lanthanum acetylacetonate-incorporated precursor solutions, respectively. The morphologies of pristine and La-doped $CsPbI_3$ NCs were characterized by transmission electron microscopy (TEM) as shown in Fig. 2. It was that the pristine

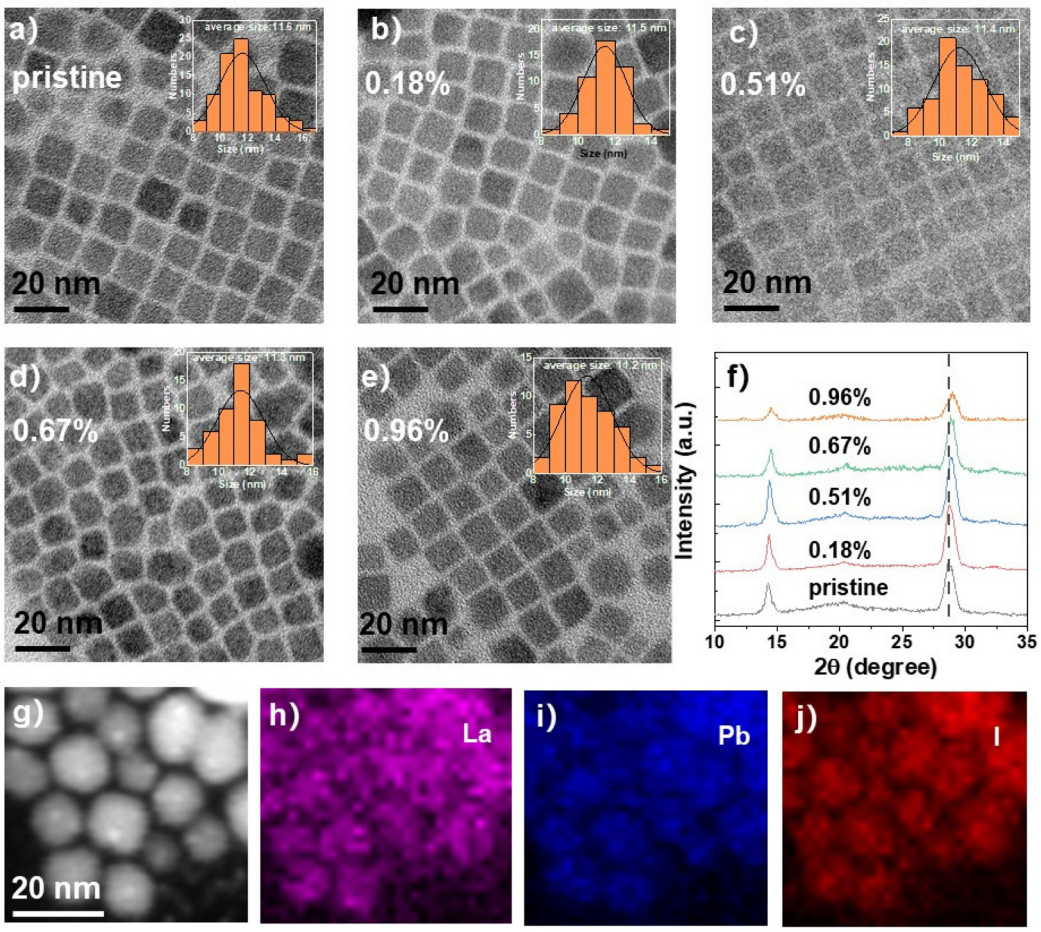

Fig. 2 Transmission electron microscopy (TEM) images of pristine and La-doped $CsPbI_3$ NCs: (a) pristine, (b) 0.18%, (c) 0.51%, (d) 0.67%, and (e) 0.96% La-doped $CsPbI_3$ NCs and (f) their corresponding X-ray diffraction (XRD) patterns. Energy-dispersive X-ray spectroscopy (EDS) element mappings of (h) La, (i) Pb, and (j) I of 0.51% La-doped $CsPbI_3$ NCs from the selected area of (g).

$CsPbI_3$ NCs exhibit a cubic shape with an average size of 11.6 nm. When increasing the ratio of La to Pb from 0.18 to 0.96%, the doped $CsPbI_3$ NCs retained reasonable mono-dispersity and cubic morphology. In contrast, the NC average size slightly declined to 11.2 nm when the La ratio reached 0.96%, which can be ascribed to the induced lattice contraction by the partial substitution of Pb with La as verified by X-ray diffraction (XRD) patterns (Fig. 2f). The characteristic diffraction peaks at 14.23° and 28.66° for pristine NCs are assigned to the (100) and (200) planes of cubic $CsPbI_3$ NCs, respectively. These peaks continuously shift to high angles with the increase in La ratio from 0.18 to 0.96%, showing the reduced interplanar crystal spacing by lattice contraction. Meanwhile, it was found that the diffraction peak intensity declined when the La ratio exceeded 0.51%, indicating the deteriorating crystalline quality of the doped NCs. Besides, no extra peaks were found in the XRD patterns after La doping, showing that the cubic crystal phase for the $CsPbI_3$ NCs remained unchanged. Furthermore, there was a good distribution of La in La-doped $CsPbI_3$ NCs as detected by energy-dispersive X-ray spectroscopy (EDS) element mapping in Fig. 2h.

The ultraviolet-visible (UV–vis) absorption and photoluminescence (PL) spectra of $CsPbI_3$ NCs doped with different concentrations of La were measured. As shown in Fig. 3a, both the absorption band edge and PL peak showed continuous blue-shifts with the La ratio increasing from 0.18 to 0.96%. In detail, the pristine NCs exhibited the PL peak centered at 690 nm, which shifted to lower wavelengths of 688, 687, 685, and 683 nm for 0.18, 0.51, 0.67, and 0.96% La-doped NCs, respectively. The blue shifts of the absorption and PL spectra for La-doped NCs were induced by the enlarged E_g due to the lattice contraction with La doping as also found in other small-sized metal-doped NCs reported previously.[40,41] The NC PLQY variations have been also monitored (Fig. 3b and S1†), in which the PLQY value increased from 70.1% (pristine) to 94.4% for 0.18% La-doped NCs, indicating enhanced carrier radiative recombination after La doping. When 0.51% La was doped into the NCs, the PLQY value further increased to near unity at 99.3%, representing one of the highest PLQYs for reported $CsPbI_3$ NCs.[27,31–35,37] The PLQY began to decline at higher ratios than 0.51% and the value decreased to 74.6 and 34.7% for 0.67 and 0.96% La-doped NCs, respectively, which was attributed to the induced poor crystalline phase at high La ratios as verified by the weakened XRD peak intensities (Fig. 2f).

To reveal the carrier radiative recombination process for the La-doped $CsPbI_3$ NCs, the time-resolved PL (TRPL) spectra of the NCs were measured and recorded in Fig. 3c. The TRPL decay curves can be well fitted by a bi-exponential function of $I(t) = a_1 \exp(-t/\tau_1) + a_2 \exp(-t/\tau_1)$, where a_1 and a_2 are the amplitudes, and τ_1 and τ_2 represent time constants for fast and slow decay lifetimes, respectively.[42] As reported previously, the fast decay lifetime (τ_1) is associated with the nonradiative recombination of the traps, and the slow decay time (τ_2) is related to the radiative recombination.[43,44] The fitted parameters for TRPL decay curves were extracted and are listed in Table S2.† It was revealed that when the La doping ratio increased from 0 to 0.51%, both τ_1 and τ_2 values greatly increased, which promotes a large enhancement of the average lifetime (τ_{avg}) from 75.82 (pristine) to 233.26 ns for 0.51% La-

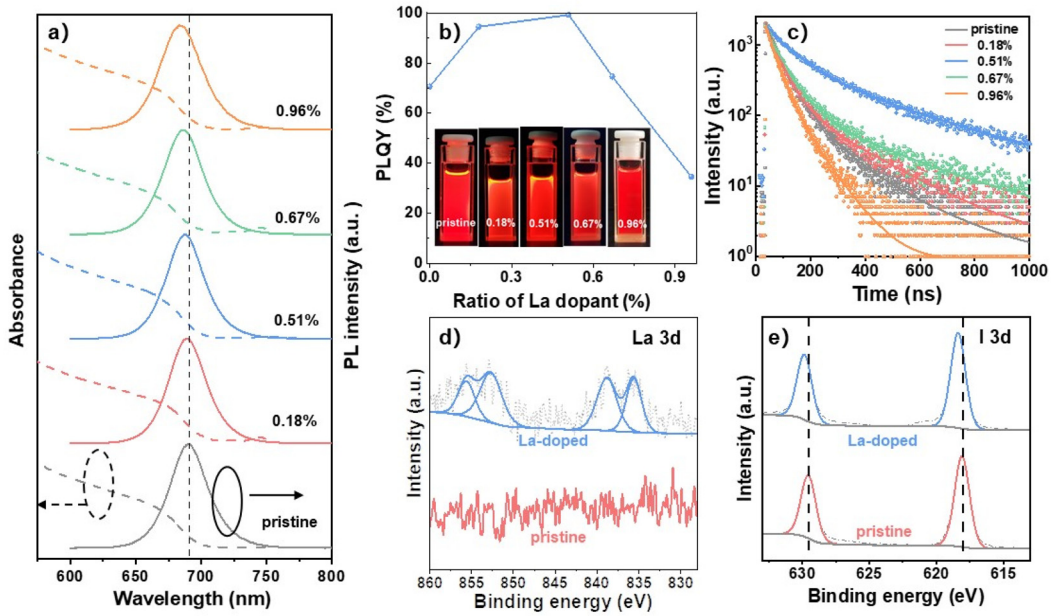

Fig. 3 (a) UV–visible absorption spectra and steady-state photoluminescence spectra, (b) photoluminescence quantum yields (PLQYs) (inset: the pictures of $CsPbI_3$ NC solutions under UV lamp), and (c) the time-resolved photoluminescence (TRPL) decay curves of pristine and La-doped NCs based on different La ratios. X-ray photoelectron spectroscopy (XPS) measurements of (d) La 3d and (e) I 3d signals for pristine and 0.51% La-doped NCs.

doped NCs, suggesting the reduced trap states for massive radiative recombination. The average lifetime declined at larger doping ratios than 0.51%, which is consistent with the trend observed in PLQY recession due to the deteriorated crystallinity (Fig. 2f) for increased non-radiative recombination. It was also found that the contribution of the fast decay component greatly decreased from 61.5% (pristine NCs) to 37.8% for 0.51% La-doped NCs, accompanied by a dramatic increase in the slow decay component from 38.5% (pristine NCs) to 62.2% (0.51% La). The results show the effectively suppressed nonradiative recombination and strengthened radiative recombination for 0.51% La-doped NCs, which can be attributed to the strong interaction between La and I ions for the suppression of traps induced by iodine loss. To analyze the interaction between La and I ions, X-ray photoelectron spectroscopy (XPS) measurements were performed on pristine and 0.51% La-doped NCs. As shown in Fig. 3d, the pristine NCs showed no signals in the detection range, while several characteristic peaks assigned to La $3d_{3/2}$ (855.68 and 852.83 eV) and $3d_{5/2}$ (838.87 and 835.60 eV) signals were observed for the La-doped NCs, indicating the successful doping of La into the NCs. Meanwhile, the binding energies of Cs 3d and Pb 4f signals remained unchanged for La-doped NCs, indicating no interaction between La and Cs or Pb (Fig. S2†). In contrast, the peaks at 629.56 and 618.11 eV ascribed to the I $3d_{3/2}$ and $3d_{5/2}$ in pristine NCs shifted to higher binding energies of 629.92 and 618.41 eV for La-doped NCs, respectively (Fig. 3e). The increased binding energy indicates the reduced electron density of I due to the electron donation from I to the La cation. The XPS results verified the strong interaction between La and I ions, which played a vital role in inhibiting the loss of I for suppressed trap states and promoting high PLQYs as discussed above.

The pristine $CsPbI_3$ NCs are inclined to transform into the non-photoactive phase under an atmospheric environment due to the serious structural distortion induced by the low tolerance factor. The environmental stability of the La-doped NCs has been measured to determine the effects of La-doping on the NC phase stability. The PLQY variations with exposure time were recorded at the temperature of 25 °C and humidity of 60% RH (Fig. 4a). The initial PLQYs for pristine and La-doped NCs were 74.3 and 98.6%, respectively. As observed, the pristine NCs exhibited poor stability against the environment with the PLQYs sharply declining to 48.1% of the initial value within 72 h, then the PLQYs further decreased to 31.9% of the initial value after exposure to the atmospheric environment for 170 h. The PLQYs of La-doped NCs declined slowly with extending the exposure time and retained 86.7% of the initial value after enduring the environmental erosion for 170 h, indicating decent environmental stability for La-doped NCs. Consistently, impure crystal phases were found for pristine NCs during the environmental stability test as verified by the appearance of massive extra XRD peaks and severe fluorescence quenching (Fig. 4b), indicating the easy phase transition of pristine NCs against the environmental surroundings. In contrast, the La-doped NCs maintained the cubic phase without significant variation of the XRD peaks after the environmental stability test (Fig. 4c). The La-doped NC solution still exhibited a bright fluorescence image, showing good stability against environmental erosion. Besides, the thermal stability of pristine and La-doped NCs was also detected by heating the NC films at gradually increasing temperatures

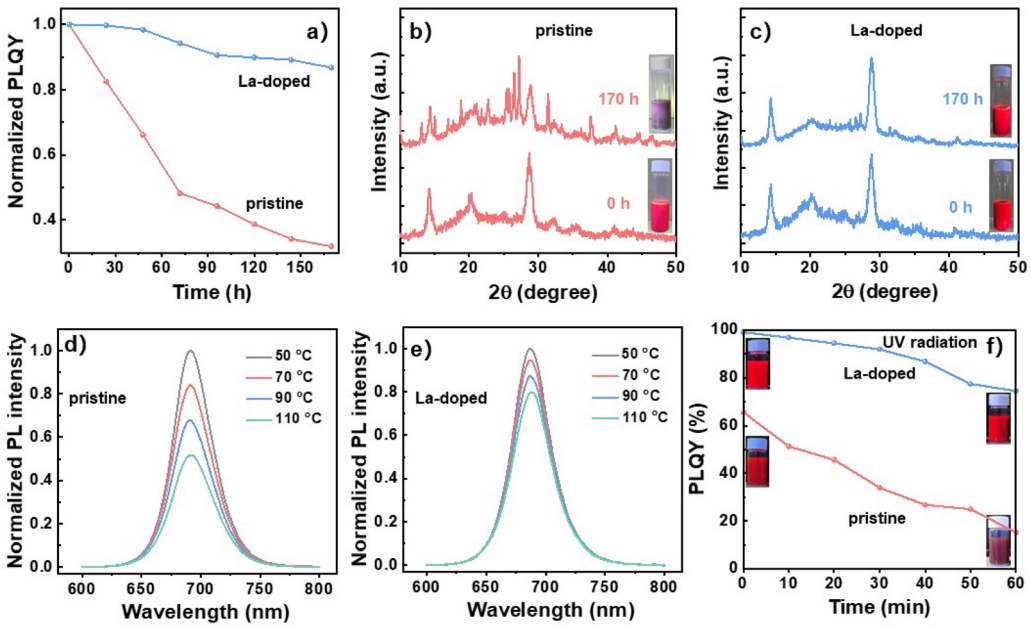

Fig. 4 (a) The environmental stability testing of pristine and 0.51% La-doped NCs and (b and c) their corresponding XRD patterns (inset: the fluorescence pictures of $CsPbI_3$ NC solutions under UV lamp). (d and e) The thermal and (f) continuous UV radiation (365 nm, 15 W) stability test of the pristine and 0.51% La-doped NCs (inset: the fluorescence pictures of $CsPbI_3$ NC solutions before and after UV irradiation).

from 50 to 110 °C. It was found that the PL intensity of pristine NC films declined dramatically with raising the heating temperatures, which decreased to 51.9% of the initial intensity after being heated at 110 °C for 10 min (Fig. 4d). The La-doped NC films showed a much slower decrease rate in PL intensity with respect to the pristine NC films (Fig. 4e). The PL intensity retained 80.2% of the initial intensity after the treatment at 110 °C for 10 min, indicating good stability for La-doped NC films to endure the heating process. The XRD patterns of pristine and La-doped NCs during thermal stability were also measured (Fig. S3†), where a phase transition from α-$CsPbI_3$ to γ-$CsPbI_3$ was observed for pristine perovskite as verified by the split peaks with increasing temperatures from 50 to 110 °C. The La-doped NCs retained constant diffraction peaks of the cubic phase during the test, indicating good phase stability after La doping. The NC stability under UV radiation (365 nm, 15 W) was also examined (Fig. 4f), in which the La-doped NCs showed decent tolerance to UV radiation. In detail, the PLQYs of pristine NCs decreased dramatically from the initial value of 65.7 to 15.1% (*i.e.*, decline to 23.0% of the initial value) after being exposed to continuous laser radiation for 60 min, indicating the severe degradation of the NCs as verified by the weakened fluorescence image of the NC solution after laser radiation (inset of Fig. 4f). The PLQYs of La-doped NCs showed a slow decline rate under UV radiation and retained 75.1% of the initial PLQY of 99.1% after exposure to UV radiation for 60 min. Meanwhile, the NC solution still presented a bright emission after the test, showing good stability against UV radiation. Consequently, we demonstrated decent environmental and thermal stability and good tolerance to UV light radiation for La-doped NCs, which can be ascribed to the diminished structure distortion and enlarged formation energy induced by the substitution of Pb with La, as well as the strengthened interaction between La and I for suppressed trap states. The superior optical properties of La-doped NCs will be beneficial for high device performance for the fabricated PeLEDs as discussed in the following section.

Since the 0.51% La-doped NCs have superior optical properties to those of the pristine NCs, we further fabricated the PeLEDs to evaluate their electroluminescence (EL) performances. The PeLEDs were assembled with the structure of ITO/poly-(ethylenedioxythiophene):polystyrenesulfonate (PEDOT:PSS)/poly(*N*,*N*′-bis-4-butylphenyl-*N*,*N*′-bisphenyl)benzidine (poly-TPD)/NCs/1,3,5-benzinetriyl-tris(1-phenyl-1-*H*-benzimidazole) (TPBi)/LiF/Al, where PEDOT:PSS, poly-TPD, NCs, and TPBi are the hole injection layer (HIL), hole transport layer (HTL), emission layer, and electron injection layer (EIL), respectively.[45,46] In the device structure, the NC emission layer is sandwiched between the poly-TPD HTL and TPBi EIL. The thicknesses of the HIL/HTL, NC emission layer, EIL, and Al cathode were around 47, 45, 41, and 70 nm, respectively, characterized by the device's cross-sectional scanning electron microscopy (SEM) image (Fig. 5a). The energy band of each functional layer of the PeLEDs is summarized in Fig. 5b, where the La-doped NCs have higher energy bands than that of pristine NCs, determined by ultraviolet photoelectron spectroscopy (UPS) (Fig. S4†). The increased energy levels for La-doped NCs facilitate the hole injection by narrowing down the energy barrier as further verified by the large injected current density of the La-doped NC-based hole-only device (Fig. S5†). The efficient hole injection promoted the distinct reduction of turn-on voltage (defined as the voltage at the luminance of 1 cd m^{-2}) from around 5.5 V (pristine) to 4.9 V for La-doped PeLEDs (Fig. 5d). Besides, the La-doped PeLEDs exhibited the maximum luminance of 592 cd m^{-2} at a bias of 7.6 V, which is an over 9-fold increase from 62 cd m^{-2} (pristine PeLEDs), suggesting the greatly increased carrier radiative recombination in La-doped PeLEDs. Consistently, the efficient radiative recombination in La-doped PeLEDs prompts a 5-fold improvement in EQE from 1.19% (pristine PeLEDs) to 6.01% (Fig. 5e). To clarify the carrier radiative recombination in the PeLEDs, the capacitance–voltage (*C*–*V*) characterizations of the devices were measured. As shown in Fig. 5f, the capacitance improves with the increase in bias voltage due to the injected charges into the PeLEDs. It was found that the La-doped PeLEDs showed a faster increase in capacitance than the pristine device, suggesting that more charges were injected into La-doped PeLEDs. At high bias, the peak capacitance sharply declined due to the greatly increased quantity of recombined electrons and holes for light emission.[47,48] The La-doped PeLEDs showed a faster decrease rate in capacitance than that of the pristine device, indicating more efficient radiative recombination of the charges, which is in good agreement with the enhanced performance of the La-doped PeLEDs.

The EL spectra in Fig. 5g show the peaks centered at 690 and 693 nm for the pristine and La-doped PeLEDs, respectively, which slightly shifted to higher wavelengths of 687 and 690 nm due to the quantum-limited Stark effect[49] (*i.e.*, in the process of device operation, the quantum dots are in an electric field that induces the energy band tilting of the quantum dots, thus leading to the decline in the quantum energy levels of electrons and holes for red-shifted luminescence peaks). The La-doped PeLEDs exhibited much stronger EL intensity than the pristine device due to the strengthened radiative recombination. The narrow band emission with the full width at half-maximum (fwhm) of around 32 nm for the La-doped PeLEDs enabled a good color purity with Commission Internationale de L'Eclairage (CIE) chromaticity coordinates at (0.72, 0.28) (Fig. S6†). The La-doped PeLEDs showed good spectral stability during the test, in which the EL peak wavelength (690 nm) and fwhm (~32 nm) remained unchanged despite the continuous increase in bias voltages from 5.5 to 8.0 V (Fig. S7†). Besides, the operational stability of the devices was further evaluated by driving the PeLEDs with a continuous constant current (Fig. 5h). Typically, the lifetime of the device is defined as the elapsed time of the device decaying to half of the initial luminance (L_0). It was found that the La-doped PeLEDs exhibited an impressive lifetime of 2956 s with an initial luminance of 109 cd m^{-2}, which is over two-fold longer than that of 1451 s for pristine PeLEDs (L_0, 103 cd m^{-2}), benefitting from the more stable phase of La-doped NCs for prolonged operational stability. Consequently, the results showed great improvements in EL

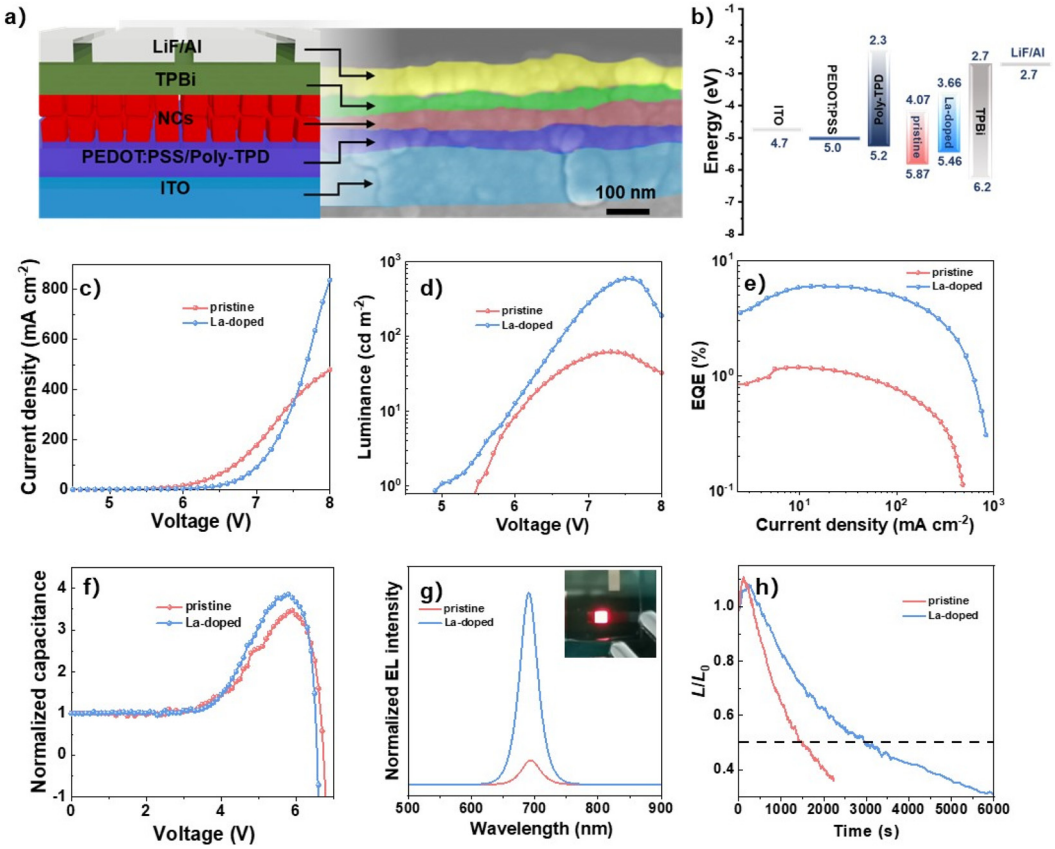

Fig. 5 (a) Device structure and cross-sectional SEM image of the PeLEDs. (b) Energy level diagram showing each functional layer of the PeLEDs. (c) Current density–voltage (*J*–*V*), (d) luminance–voltage (*L*–*V*), (e) efficiency–current density (EQE–*J*), and (f) capacitance–voltage (*C*–*V*) plots for pristine and La-doped PeLEDs. (g) The EL spectra of the devices (inset: the emission image of La-doped PeLEDs). (h) The lifetime measurements of pristine and La-doped PeLEDs with the initial brightness of 109 and 103 cd m^{-2} under constant currents of 125.0 and 50.0 mA cm^{-2}, respectively.

performance with high brightness, large EQE, and long operational stability for La-doped PeLEDs, addressing the important role of La doping for efficient PeLEDs.

Conclusions

In summary, we have successfully synthesized La-doped $CsPbI_3$ NCs to fundamentally improve the phase stability by reducing the structural distortion to achieve high endurance to the environment, heat, and UV radiation. Meanwhile, the strong interaction between La and I of the octahedra enables the effective suppression of the trap states induced by iodide loss for massive carrier radiative recombination and thus high emission efficiency. By optimizing the dopant ratio, we demonstrated excellent optical properties for 0.51% La-doped NCs with a near-unity PLQY of 99.3%, which represents one of the highest values reported. The narrowed energy barrier for hole injection was also demonstrated for the La-doped NCs by increasing the energy levels. These superior optoelectronic properties of La-doped NCs promote high-performance red PeLEDs with more than a 9-fold increase in luminance from 62 to 592 cd m^{-2}, 5-fold improvement in EQE from 1.19 to 6.01%, and two-fold longer lifetime from 1451 to 2956 s for La-doped PeLEDs. Consequently, this work paves an effective way for rare earth metal ion doping to realize phase-stable $CsPbI_3$ NCs for high-performing PeLEDs.

Experimental section

Materials

Octadecene (ODE, 90%) and oleic acid (OA, 90%) were purchased from Alfa Aesar. Oleylamine (OAm), methyl acetate (MeOAc, 99%), *n*-octane (99%), and lanthanum acetylacetonate ($La(acac)_3$, 99.99%) were purchased from J&K Scientific. Cesium carbonate (Cs_2CO_3, 99.99%) was purchased from Aladdin. Lead iodide (PbI_2) and poly-(ethylenedioxythiophene):polystyrenesulfonate (PEDOT:PSS, Al4083) were purchased from Xi'an Polymer Light Technology Corp. Poly(*N*,*N*′-bis-4-butylphenyl-*N*,*N*′-bisphenyl)benzidine (poly-TPD) was purchased from American Dye Source.

Synthesis of Cs–OA precursor

Cs_2CO_3 (814 mg), OA (2.5 mL), and ODE (30 mL) were loaded into a 100 mL three-necked flask and dried at 120 °C under

vacuum for 1 h. The mixture was heated to 150 °C under N_2 protection to fully dissolve the Cs_2CO_3 powder. The Cs–OA precursor was obtained by cooling the solution, which was stored in the glove box before use.

Synthesis of pristine and La-doped $CsPbI_3$ NCs

PbI_2 (173 mg) and ODE (10 mL) were added to a 50 mL three-necked flask. For the synthesis of La-doped $CsPbI_3$ NCs, extra $La(acac)_3$ with different mole ratios to PbI_2 was added into the flask. The mixture was heated to 120 °C under a vacuum for 1 h. The pre-dried OA (1 mL) and OAm (1 mL) were injected under the protection of N_2. Subsequently, the mixture was further heated to 165 °C followed by injecting the pre-warmed Cs–OA precursor (1 ml). After 5 s, the reaction solution was quickly cooled by immersing the flask in an ice-water bath. The purification process was carried out by adding the appropriate amount of MeOAc to the crude solution. After purification twice, the NCs were re-dispersed in *n*-octane before use.

Device fabrication

The indium tin oxide (ITO) glass substrates were successively cleaned with deionized water, acetone, and isopropanol. The cleaned substrates were further treated with UV-ozone for 15 min to improve surface hydrophilicity. Then PEDOT:PSS was spin-coated on the substrates at 4000 rpm for 40 s and annealed at 150 °C in the air for 20 min. After that, the substrates were transferred into a nitrogen-filled glove box. The poly-TPD solution (8 mg mL^{-1} in chlorobenzene) was spin-coated at 4000 rpm for 40 s and annealed at 140 °C for 30 min. The $CsPbI_3$ NCs solution was spin-coated at 2000 rpm for 60 s to prepare the emission layer. Subsequently, TPBi (45 nm), LiF (1 nm), and Al (100 nm) were deposited at the deposition rate of 0.4, 0.03, and 1 Å s^{-1} by thermal evaporation under a vacuum of 5×10^{-4} Pa to complete the device fabrication process.

Characterization

The calculations of the density of states for both pristine and La-doped $CsPbI_3$ supercells were performed with the Vienna *ab initio* Simulation Package (VASP). The DFT calculations were mainly based on the method of generalized gradient approximation (GGA) and the Perdew–Burke–Ernzerhof (PBE) exchange–correlation function. The cutoff energy was set to 500 eV. The atomic positions were fully optimized until the forces on the atoms were below 0.05 eV $Å^{-1}$. The convergence threshold for self-consistent-field (SCF) iteration was set at 10^{-6} eV. The X-ray diffraction patterns were obtained with the use of an X-ray diffractometer of Bruker D8 Advance (Cu Kα radiation, λ = 1.54 Å). TEM images were obtained by an FEI Tecnai G20 S-TWIN TMP microscope operating at an accelerating voltage of 200 kV. EDS elemental mapping was obtained using an FEI Talos F200X microscope. The XPS and UPS measurements were carried out using the equipment of Thermo Fisher Escalab 250Xi. Time-resolved PL spectra were acquired using an Edinburgh FLS 1000 fluorescence spectrophotometer equipped with a picosecond pulse laser (375 nm) with a pulse width of 50 ps. The spectra were recorded by a time-corrected single-photon counting of the TCSPC (PicoHarp 300E) module equipped with a photomultiplier (PMT-900) detector. The UV–vis spectroscopy was conducted with a PerkinElmer spectrophotometer (Lambda 750S). The PLQY values of the perovskite films were obtained using a spectrofluorometer of Edinburgh FS5. The PeLED performances were measured by an Ocean Optics system, which consists of a source meter (Keithley 2450), a spectrometer (QE Pro), and an integrating sphere (FOIS-1). To minimize the effects of the ambient atmosphere on the measurements, the samples were prepared in a nitrogen-filled glove box and then sealed in a nitrogen-filled glass box before XRD, XPS, and UPS testing. The PeLEDs were sealed with an ultraviolet-curable resin before testing.

Author contributions

W. Xia performed the experiments and wrote the draft of the manuscript; Z. Ren analyzed the results and revised the manuscript; Z. Zheng, C. Luo, J. Li, and W. Ma prepared the sample characterizations; X. Zhou assisted in the device fabrication; Y. Chen supervised the whole project.

Conflicts of interest

The authors declare no conflict of interest.

Acknowledgements

This research was supported by the National Key R&D Program of China (Grant No. 2022YFB3608200 and 2021YFB2802201), the National Natural Science Foundation of China (Grant No. 62275183 and 62105231), the Natural Science Foundation of Jiangsu Province of China (Grant No. BK20210712), the Natural Science Foundation of the Jiangsu Higher Education Institutions of China (19KJA550001), Key Lab of Modern Optical Technologies of Education Ministry of China, Key Lab of Advanced Optical Manufacturing Technologies of Jiangsu Province, Priority Academic Program Development (PAPD) of Jiangsu Higher Education Institutions, and Jiangsu Shuang Chuang Plan.

References

1 Q. A. Akkerman, G. Raino, M. V. Kovalenko and L. Manna, *Nat. Mater.*, 2018, **17**, 394–405.
2 J. Shamsi, A. S. Urban, M. Imran, L. De Trizio and L. Manna, *Chem. Rev.*, 2019, **119**, 3296–3348.
3 X. K. Liu, W. Xu, S. Bai, Y. Jin, J. Wang, R. H. Friend and F. Gao, *Nat. Mater.*, 2021, **20**, 10–21.

4 J. Chen, J. Wang, X. Xu, J. Li, J. Song, S. Lan, S. Liu, B. Cai, B. Han, J. T. Precht, D. Ginger and H. Zeng, *Nat. Photonics*, 2021, **15**, 238–244.
5 Y. Zhai, X. Bai, G. Pan, J. Zhu, H. Shao, B. Dong, L. Xu and H. Song, *Nanoscale*, 2019, **11**, 2484–2491.
6 J. Song, T. Fang, J. Li, L. Xu, F. Zhang, B. Han, Q. Shan and H. Zeng, *Adv. Mater.*, 2018, **30**, 1805409.
7 Y. K. Wang, F. Yuan, Y. Dong, J. Y. Li, A. Johnston, B. Chen, M. I. Saidaminov, C. Zhou, X. Zheng, Y. Hou, K. Bertens, H. Ebe, D. Ma, Z. Deng, S. Yuan, R. Chen, L. K. Sagar, J. Liu, J. Fan, P. Li, X. Li, Y. Gao, M. K. Fung, Z. H. Lu, O. M. Bakr, L. S. Liao and E. H. Sargent, *Angew. Chem., Int. Ed.*, 2021, **60**, 16164–16170.
8 Y. Dong, Y. K. Wang, F. Yuan, A. Johnston, Y. Liu, D. Ma, M. J. Choi, B. Chen, M. Chekini, S. W. Baek, L. K. Sagar, J. Fan, Y. Hou, M. Wu, S. Lee, B. Sun, S. Hoogland, R. Quintero-Bermudez, H. Ebe, P. Todorovic, F. Dinic, P. Li, H. T. Kung, M. I. Saidaminov, E. Kumacheva, E. Spiecker, L. S. Liao, O. Voznyy, Z. H. Lu and E. H. Sargent, *Nat. Nanotechnol.*, 2020, **15**, 668–674.
9 Z. Liu, W. Qiu, X. Peng, G. Sun, X. Liu, D. Liu, Z. Li, F. He, C. Shen, Q. Gu, F. Ma, H. L. Yip, L. Hou, Z. Qi and S. J. Su, *Adv. Mater.*, 2021, **33**, 2103268.
10 F. Zhou, Z. Li, H. Chen, Q. Wang, L. Ding and Z. Jin, *Nano Energy*, 2020, **73**, 104757.
11 X. Wu, H. Shao, Y. Zhong, L. Li, W. Chen, B. Dong, L. Xu, W. Xu, D. Zhou, Z. Wu, H. Song and X. Bai, *Small*, 2022, **18**, 2106147.
12 B. Saparov and D. B. Mitzi, *Chem. Rev.*, 2016, **116**, 4558–4596.
13 Z. Yao, W. Zhao and S. Liu, *J. Mater. Chem. A*, 2021, **9**, 11124–11144.
14 L. Xu, H. W. Liang, Y. Yang and S. H. Yu, *Chem. Rev.*, 2018, **118**, 3209–3250.
15 A. Swarnkar, A. R. Marshall, E. M. Sanehira, B. D. Chernomordik, D. T. Moore, J. A. Christians, T. Chakrabarti and J. M. Luther, *Science*, 2016, **354**, 92–95.
16 J. Shi, F. Li, Y. Jin, C. Liu, B. Cohen-Kleinstein, S. Yuan, Y. Li, Z. K. Wang, J. Yuan and W. Ma, *Angew. Chem., Int. Ed.*, 2020, **59**, 22230–22237.
17 Y. Hassan, J. H. Park, M. L. Crawford, A. Sadhanala, J. Lee, J. C. Sadighian, E. Mosconi, R. Shivanna, E. Radicchi, M. Jeong, C. Yang, H. Choi, S. H. Park, M. H. Song, F. De Angelis, C. Y. Wong, R. H. Friend, B. R. Lee and H. J. Snaith, *Nature*, 2021, **591**, 72–77.
18 E. Hassanabadi, M. Latifi, A. F. Gualdron-Reyes, S. Masi, S. J. Yoon, M. Poyatos, B. Julian-Lopez and I. Mora-Sero, *Nanoscale*, 2020, **12**, 14194–14203.
19 J. Kim, S. Cho, F. Dinic, J. Choi, C. Choi, S. M. Jeong, J.-S. Lee, O. Voznyy, M. J. Ko and Y. Kim, *Nano Energy*, 2020, **75**, 104985.
20 B. Li, Y. Zhang, L. Fu, T. Yu, S. Zhou, L. Zhang and L. Yin, *Nat. Commun.*, 2018, **9**, 1076.
21 K. Sun, D. Tan, J. Song, W. Xiang, B. Xu and J. Qiu, *Adv. Opt. Mater.*, 2021, **9**, 2100094.
22 Y. Ji, M. Wang, Z. Yang, H. Qiu, S. Ji, J. Dou and N. V. Gaponenko, *Nanoscale*, 2020, **12**, 6403–6410.
23 X. Ma, L. Yang, K. Lei, S. Zheng, C. Chen and H. Song, *Nano Energy*, 2020, **78**, 105354.
24 A. Kausar, A. Sattar, C. Xu, S. Zhang, Z. Kang and Y. Zhang, *Chem. Soc. Rev.*, 2021, **50**, 2696–2736.
25 R. J. Sutton, G. E. Eperon, L. Miranda, E. S. Parrott, B. A. Kamino, J. B. Patel, M. T. Hörantner, M. B. Johnston, A. A. Haghighirad, D. T. Moore and H. J. Snaith, *Adv. Energy Mater.*, 2016, **6**, 1502458.
26 L. Hu, X. Guan, W. Chen, Y. Yao, T. Wan, C.-H. Lin, N. D. Pham, L. Yuan, X. Geng, F. Wang, C.-Y. Huang, J. Yuan, S. Cheong, R. D. Tilley, X. Wen, D. Chu, S. Huang and T. Wu, *ACS Energy Lett.*, 2021, **6**, 1649–1658.
27 Q. Chen, S. Cao, K. Xing, M. Ning, R. Zeng, Y. Wang and J. Zhao, *J. Phys. Chem. Lett.*, 2021, **12**, 11090–11097.
28 M. Liu, N. Jiang, H. Huang, J. Lin, F. Huang, Y. Zheng and D. Chen, *Chem. Eng. J.*, 2021, **413**, 127547.
29 R. K. Behera, A. Dutta, D. Ghosh, S. Bera, S. Bhattacharyya and N. Pradhan, *J. Phys. Chem. Lett.*, 2019, **10**, 7916–7921.
30 L. Zhang, C. Kang, G. Zhang, Z. Pan, Z. Huang, S. Xu, H. Rao, H. Liu, S. Wu, X. Wu, X. Li, Z. Zhu, X. Zhong and A. K. Y. Jen, *Adv. Funct. Mater.*, 2020, **31**, 2005930.
31 X. Shen, Y. Zhang, S. V. Kershaw, T. Li, C. Wang, X. Zhang, W. Wang, D. Li, Y. Wang, M. Lu, L. Zhang, C. Sun, D. Zhao, G. Qin, X. Bai, W. W. Yu and A. L. Rogach, *Nano Lett.*, 2019, **19**, 1552–1559.
32 W. Shen, J. Zhang, R. Dong, Y. Chen, L. Yang, S. Chen, Z. Su, Y. Dai, K. Cao, L. Liu, S. Chen and W. Huang, *Research*, 2021, **2021**, 9829374.
33 C. Chen, T. Xuan, W. Bai, T. Zhou, F. Huang, A. Xie, L. Wang and R. J. Xie, *Nano Energy*, 2021, **85**, 106033.
34 J. S. Yao, J. Ge, K. H. Wang, G. Zhang, B. S. Zhu, C. Chen, Q. Zhang, Y. Luo, S. H. Yu and H. B. Yao, *J. Am. Chem. Soc.*, 2019, **141**, 2069–2079.
35 H. Li, H. Lin, D. Ouyang, C. Yao, C. Li, J. Sun, Y. Song, Y. Wang, Y. Yan, Y. Wang, Q. Dong and W. C. H. Choy, *Adv. Mater.*, 2021, **33**, 2008820.
36 S. M. Yoon, H. Min, J. B. Kim, G. Kim, K. S. Lee and S. I. Seok, *Joule*, 2021, **5**, 183–196.
37 B. Shu, Y. Chang, J. Zhang, X. Cheng and D. Yu, *Nano Res.*, 2021, **14**, 3352–3357.
38 D. Liu, W. Zha, Y. Guo and R. Sa, *ACS Omega*, 2020, **5**, 893–896.
39 A. A. Emery and C. Wolverton, *Sci. Data*, 2017, **4**, 170153.
40 S. Zhang, H. Liu, X. Li and S. Wang, *Nano Energy*, 2020, **77**, 105302.
41 G. Pan, X. Bai, W. Xu, X. Chen, Y. Zhai, J. Zhu, H. Shao, N. Ding, L. Xu, B. Dong, Y. Mao and H. Song, *ACS Appl. Mater. Interfaces*, 2020, **12**, 14195–14202.
42 Z. Ren, X. Xiao, R. Ma, H. Lin, K. Wang, X. W. Sun and W. C. H. Choy, *Adv. Funct. Mater.*, 2019, **29**, 1905339.
43 L. Zhang, X. Yang, Q. Jiang, P. Wang, Z. Yin, X. Zhang, H. Tan, Y. M. Yang, M. Wei, B. R. Sutherland, E. H. Sargent and J. You, *Nat. Commun.*, 2017, **8**, 15640.

44 Z. Ren, J. Sun, J. Yu, X. Xiao, Z. Wang, R. Zhang, K. Wang, R. Chen, Y. Chen and W. C. H. Choy, *Nano-Micro Lett.*, 2022, **14**, 66.
45 D. Shen, Z. Ren, Q. Li, C. Luo, W. Xia, Z. Zheng, W. Ma, J. Li and Y. Chen, *ACS Appl. Mater. Interfaces*, 2022, **14**, 21636–21644.
46 Z. Ren, K. Wang, X. W. Sun and W. C. H. Choy, *Adv. Funct. Mater.*, 2021, **31**, 2100516.
47 Z. Ren, J. Yu, Z. Qin, J. Wang, J. Sun, C. C. S. Chan, S. Ding, K. Wang, R. Chen, K. S. Wong, X. Lu, W. J. Yin and W. C. H. Choy, *Adv. Mater.*, 2021, **33**, 2005570.
48 Z. Ren, L. Li, J. Yu, R. Ma, X. Xiao, R. Chen, K. Wang, X. W. Sun, W.-J. Yin and W. C. H. Choy, *ACS Energy Lett.*, 2020, **5**, 2569–2579.
49 Y. Shirasaki, G. J. Supran, M. G. Bawendi and V. Bulović, *Nat. Photonics*, 2012, **7**, 13–23.